



Chemical bonding dictates drastic critical temperature difference in two seemingly identical superconductors

Robert H. Lavroff^a, Julen Munarritz^b, Claire E. Dickerson^a, Francisco Munoz^{c,d,1}, and Anastassia N. Alexandrova^{a,e,f,1}

Edited by Laura Gagliardi, The University of Chicago, Chicago, IL; received September 21, 2023; accepted January 11, 2024

Though YB_6 and LaB_6 share the same crystal structure, atomic valence electron configuration, and phonon modes, they exhibit drastically different phonon-mediated superconductivity. YB_6 superconducts below 8.4 K, giving it the second-highest critical temperature of known borides, second only to MgB_2 . LaB_6 does not superconduct until near-absolute zero temperatures (below 0.45 K), however. Though previous studies have quantified the canonical superconductivity descriptors of YB_6 's greater Fermi-level (E_F) density of states and higher electron–phonon coupling (EPC), the root of this difference has not been assessed with full detail of the electronic structure. Through chemical bonding, we determine low-lying, unoccupied 4f atomic orbitals in lanthanum to be the key difference between these superconductors. These orbitals, which are not accessible in YB_6 , hybridize with π B–B bonds and bring this π -system lower in energy than the σ B–B bonds otherwise at E_F . This inversion of bands is crucial: the optical phonon modes we show responsible for superconductivity cause the σ -orbitals of YB_6 to change drastically in overlap, but couple weakly to the π -orbitals of LaB_6 . These phonons in YB_6 even access a crossing of electronic states, indicating strong EPC. No such crossing in LaB_6 is observed. Finally, a supercell (the M k-point) is shown to undergo Peierls-like effects in YB_6 , introducing additional EPC from both softened acoustic phonons and the same electron-coupled optical modes as in the unit cell. Overall, we find that LaB_6 and YB_6 have fundamentally different mechanisms of superconductivity, despite their otherwise near-identity.

superconductivity | chemical bonding | electron–phonon coupling | borides

The massively wide range of physical properties exhibited by rare-earth hexaborides makes them useful for a variety of applications, yet the molecular-level origins of many of these properties are poorly understood. All sharing an ambient crystal structure (Pm3m space group) of a metal surrounded by a network of boron octahedra, these ceramic compounds present themselves vastly differently as semiconductors (1–3), Kondo insulators (4–6), magnetically ordered materials (7, 8), and more (2, 9–15). Lanthanum hexaboride, though primarily exploited in hot cathodes for its high electron emissivity, is also known to be a low-temperature, Bardeen–Cooper–Schrieffer (BCS, i.e., phonon-mediated) superconductor at temperatures below 0.45 K (16). Isostructural yttrium hexaboride, possessing a near-identical phonon spectrum, a similar lattice constant (4.155 Å for LaB_6 , 4.098 Å for YB_6), and yttrium being one row directly above lanthanum in the periodic table, is a significantly better BCS superconductor at a critical temperature (T_c) of up to 8.4 K (17–19). This notably makes it the only reported superconducting hexaboride with a T_c reachable with ^4He cryogenics (20, 21). It also possesses the second-highest superconducting T_c of any metal boride (22), the highest being that of the unusual (23) and thoroughly studied MgB_2 (24–28), the highest- T_c “conventional” (i.e., phonon-mediated) superconductor.

The canonical descriptions of superconducting phase transitions via Migdal–Eliashberg (29, 30) and McMillan–Allen–Dynes (31, 32) formalisms show density of states (DOS) at the Fermi level (E_F) and electron–phonon coupling (EPC) to be the two key factors contributing to superconducting temperature, as both are descriptors for how drastically electrons in a superconductor “feel” the lattice and thus form Cooper pairs. As E_F -DOS and EPC increase, so too will T_c . Indeed, samples of YB_6 of increasing T_c have been confirmed by ^{89}Y nuclear magnetic resonance (NMR) to also have increasing E_F -DOS, and YB_6 is known through tunneling and DC magnetization (33), point-contact spectroscopy (34), and electronic Raman scattering (35), as well as Density functional theory (DFT) (36), to have moderate to strong EPC, depending on the sample.

While experimental and computational studies have been conducted to characterize the Fermi level electronic structure (3, 12, 37–41) of YB_6 and LaB_6 and their phonon modes (41–48) contributing to EPC, the linkage of the two—how frontier electronic eigenstates physically couple to these lattice vibrations—has yet to be established, as has been done with other prominent phonon-mediated superconductors (26, 27, 49). Prior

Significance

Chemical bonding is a powerful approach to materials rationalization and design due to its beauty in simplicity. As the field of quantum materials takes the scientific community by storm, an understanding of these materials (such as superconductors) in the language of chemistry is essential for complete characterization and predictive capabilities. In this work, we demonstrate such an understanding by differentiating, using only their molecular orbitals and vibrational modes, two superconductors which are expected to behave identically but are drastically different in reality. This study paves the way for a chemist's view of phonon-mediated superconductivity and opens the door to prediction of other quantum materials' behavior using chemical bonding.

Author affiliations: ^aDepartment of Chemistry and Biochemistry, University of California, Los Angeles, CA 90095; ^bDepartamento de Química Física and Instituto de Biocomputación y Física de Sistemas Complejos, Universidad de Zaragoza, Zaragoza 50009, Spain; ^cDepartamento de Física, Facultad de Ciencias, Universidad de Chile, Santiago 7800024, Chile; ^dCenter for the Development of Nanoscience and Nanotechnology, Santiago 9330111, Chile; ^eDepartment of Materials Science and Engineering, University of California, Los Angeles, CA 90095; and ^fCalifornia NanoSystems Institute, University of California, Los Angeles, CA 90095

Author contributions: R.H.L., J.M., F.M., and A.N.A. designed research; R.H.L., J.M., C.E.D., and F.M. performed research; R.H.L., J.M., F.M., and A.N.A. analyzed data; and R.H.L., F.M., and A.N.A. wrote the paper.

The authors declare no competing interest.

This article is a PNAS Direct Submission.

Copyright © 2024 the Author(s). Published by PNAS. This article is distributed under Creative Commons Attribution-NonCommercial-NoDerivatives License 4.0 (CC BY-NC-ND).

¹To whom correspondence may be addressed. Email: fmunoz@gmail.com or ana@chem.ucla.edu.

This article contains supporting information online at <https://www.pnas.org/lookup/suppl/doi:10.1073/pnas.2316101121/-DCSupplemental>.

Published March 28, 2024.

studies of our group have quantitatively and qualitatively explained properties of metal hexaborides through the lens of chemical bonding (6, 9, 50), and in this study, we extend this capability to superconducting hexaborides by analyzing changes in this bonding under phonon-induced lattice deformations.

Results

Determination of the Phonon Modes Responsible for Superconductivity. The BCS theory of superconductivity attributes the formation of Cooper pairs to lattice vibrations (phonons) pairing electrons near a material's Fermi level (E_f), ultimately forming a condensate of Cooper pairs and thus an electron flow experiencing zero resistance. In turn, the phonon modes that will form Cooper pairs by inducing a large EPC are likely those breaking the degeneracy of partially occupied electron bands at the Fermi level (51). While a number of modes in the phonon dispersion of YB_6 (Fig. 1A) and LaB_6 (Fig. 1B) can accomplish this (SI Appendix, Fig. S1 shows the effects of all 21 phonons on the electronic band structures), the modes of interest in this group are those possessing the lowest frequency, as they are likely to require the least amount of vibrational energy to break degeneracy. These flat phonon bands, circled in red at the Γ (G) points of Fig. 1, represent a Raman-active T_{2g} mode which is triply degenerate as the same motion in the x, y, and z directions of the lattice. Of the 21 phonons, they are the 13th to 15th lowest in energy (the order of the three is arbitrary) at approximately 21 THz. Fig. 1C shows a visualization of each of these vibrations (labeled i, ii, and iii) while Fig. 1D and E show how each breaks electronic degeneracy in YB_6 and LaB_6 . The other, higher-energy group of phonons which can be responsible for Cooper pairs are at 35 to 40 THz for YB_6 and 32 to 36 THz for LaB_6 (phonons 19 to 21). Although the BCS model of superconductivity allows virtual phonons (i.e., phonons too high in energy to be "occupied" vibrational quasiparticle bands) to participate in Cooper pairing, these three modes break band structure degeneracies in a near-identical manner to the phonons in Fig. 1C and are thus omitted from the remainder of this study.

All six phonons mentioned here, 13 to 15 and 19 to 21, can be visualized with an animation-like representation using the GIF or interactive files attached as SI. All six involve motion of the boron atoms only, with the metal remaining stationary. In contrast to the low-energy vibrations of the metal in the boron "cage," these sets of mid and high-energy phonons are confirmed by experimental Raman scattering of LaB_6 and YB_6 to exhibit little to no anharmonicity, as shown by their Gruneisen parameters. This same study determines EPC contributions of the anharmonic, acoustic phonons to be low and observes opposite temperature dependence of boron octahedra vibrations between YB_6 and LaB_6 , hypothesizing that these higher-frequency, optical phonons promote a higher T_c in YB_6 (48). This is consistent with our computational observation of phonons 13 to 15 and 19 to 21 being significant for superconductivity in these two materials.

The magnitude of displacement along the phonon mode in Fig. 1D and E is arbitrary and meant only to demonstrate degeneracy breaking, but it should be noted that at such low temperatures as 8.4 or 0.45 K, the only appreciable vibrational energy contributing to these displacements comes from zero-point energy (ZPE): $\frac{1}{2} \hbar \omega_{\text{phonon}}$, which corresponds to 0.04215 eV and 0.0434 eV, for YB_6 and LaB_6 , respectively. SI Appendix, Fig. S2, by plotting the ZPE line and DFT energies along the phonon distortion, shows that the classical turning points past which the lattice cannot distort are approximately 1.5 to 2.2 degrees for YB_6 and 1 to 3 degrees for LaB_6 , depending on the phonon. This angle is shown

at the *Bottom* of SI Appendix, Fig. S2 (labeled ϕ) and is given as a range because the symmetry of some of the frontier electronic bands prevents the EPC from being completely isotropic in x, y, and z directions, as discussed in the coming section. This ZPE analysis will become essential information in later discussion of chemical bonding under phonons, as YB_6 undergoes a crossing of states along the phonon-induced potential energy surface (PES) at a deformation angle of approximately 2 degrees, while LaB_6 experiences no such crossing, even up to unphysical 5 degree distortions (Fig. 3B).

Relation of Frontier Orbitals between YB_6 and LaB_6 . Fig. 1C and D demonstrate that the lattice vibrations relevant to superconductivity are "rocking" motions of the two boron atoms fusing B_6 octahedra. Our previous studies showed that these B–B bonds constitute the most significant B–B interactions in rare-earth hexaborides (6, 9). We aim to reveal how the eigenstates (orbitals) comprising the valence bands of the studied hexaborides physically couple to these vibrations. From the PDOS in Fig. 1D and E, we see that boron 2s and 2p orbitals and yttrium 4d orbitals comprise the Fermi surface of YB_6 , while boron 2s and 2p orbitals and lanthanum 5f orbitals comprise that of LaB_6 . Specifically, in both materials, all boron valence AOs (i.e., of principal quantum number 2) contribute, with additions of $4d_{x^2-y^2}$ and $4d_z$ AOs in YB_6 and $4f_{xz}^3$, $4f_{yz}^2$, $4f_{xz}^2$, $4f_{zx}^2$, and $4f_z^3$ AOs in LaB_6 . In atomic lanthanum, no electrons occupy 4f orbitals and thus it is somewhat surprising to see these states occupying LaB_6 's E_f rather than 6s or 5d. 4f orbitals, however, have been shown to enable covalency with very compact valence orbitals of boron (52). In addition, 4f AOs are bond-promiscuous in a solid because unlike 5d and 6s, which possess two and six nodes in their radial wavefunctions, they have no radial nodes and are thus not destabilized by the "chemical pressure" of a fixed lattice. By contrast, orbitals *with* radial nodes would begin to experience destructive interference when pushed together due to a sign change in wavefunction phase. For this reason, significant 4f contributions have been shown to dominate the E_f -DOS even at extreme pressures for the proposed high- T_c superconductor LaH_{10} (53). A more canonical example of this nodality phenomenon is solid beryllium being held together by hybridized 2p orbitals despite a single Be atom having only 2s valence electrons (2s orbitals have radial nodes but 2p do not) (54, 55).

In Fig. 2, we show the Kohn–Sham orbitals of our DFT calculations for each valence and conduction band, plotted specifically at the Γ point such that all unit cells' orbitals are in-phase. Unrotated Bloch orbitals, rather than Wannier functions, are plotted for their ability to describe the delocalized bonding of the metallic bulk. We henceforth refer to these orbitals in the chemistry vocabulary of highest occupied molecular orbitals (HOMO) for the valence bands and lowest unoccupied molecular orbitals (LUMO) for the conduction bands, HOMO and LUMO referred to collectively as frontier orbitals. It is valid in our study to analyze these bands at the Γ point due to the electron–phonon coupling being localized near the Γ point when plotted along the phonon dispersion. SI Appendix, Fig. S3 shows there is one other source of significant EPC coming from these same phonon bands at momentum M, which we discuss via Fermi surface analysis in the section "Additional EPC in a supercell." The bonding picture at M is similar to that at Γ , but phase relations between unit cells must be considered.

YB_6 has two degenerate valence bands and three degenerate conduction bands at and around the Γ point, while LaB_6 has the opposite degeneracies. Quite notably, the HOMO of YB_6 looks identical to the LUMO of LaB_6 . Both sets of orbitals are a system

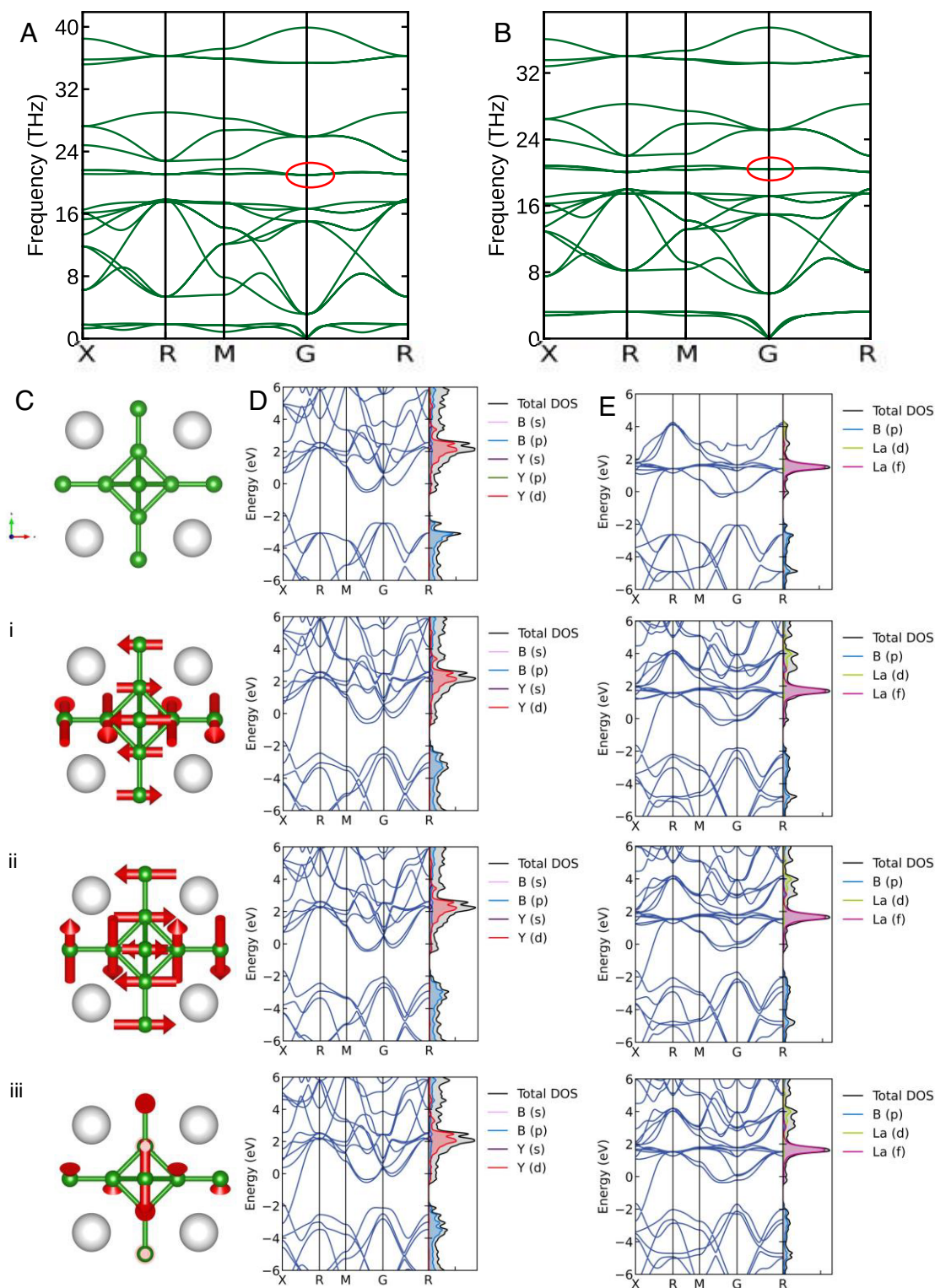


Fig. 1. Phonon dispersions of YB_6 (A) and LaB_6 (B). (C) Visualizations of the lowest energy phonons responsible for superconductivity at the Γ point in YB_6 and LaB_6 ; phonons 13 to 15. White atoms represent the metal (yttrium or lanthanum); green atoms are boron. The topmost structure, with no phonon mode arrows, represents the equilibrium geometry. (D) Effect of the three phonons applied to YB_6 on degeneracy splittings at the Fermi level. (E) Effect of the three phonons applied to LaB_6 on degeneracy splittings at the Fermi level.

of metal-metal and B–B σ -bonds extending along the x , y , and z lattice vectors of the unit cell. They are doubly, rather than triply degenerate, however, due to the d_z^2 and $d_{x^2-y^2}$ AOs forming the metal–metal bond possessing E_g symmetry. Additionally, the LUMO of YB_6 looks identical to the triply degenerate HOMO

of LaB_6 , absent bonding involvement of the metal in YB_6 . This is a system of π -bonds on octahedra-fusing boron dimers which link unit cells, and in the case of LaB_6 HOMO, $4f$ electron density hybridizes with this π system as well. Greater in-phase overlap of molecular orbitals lowers their energy, and thus it can be readily

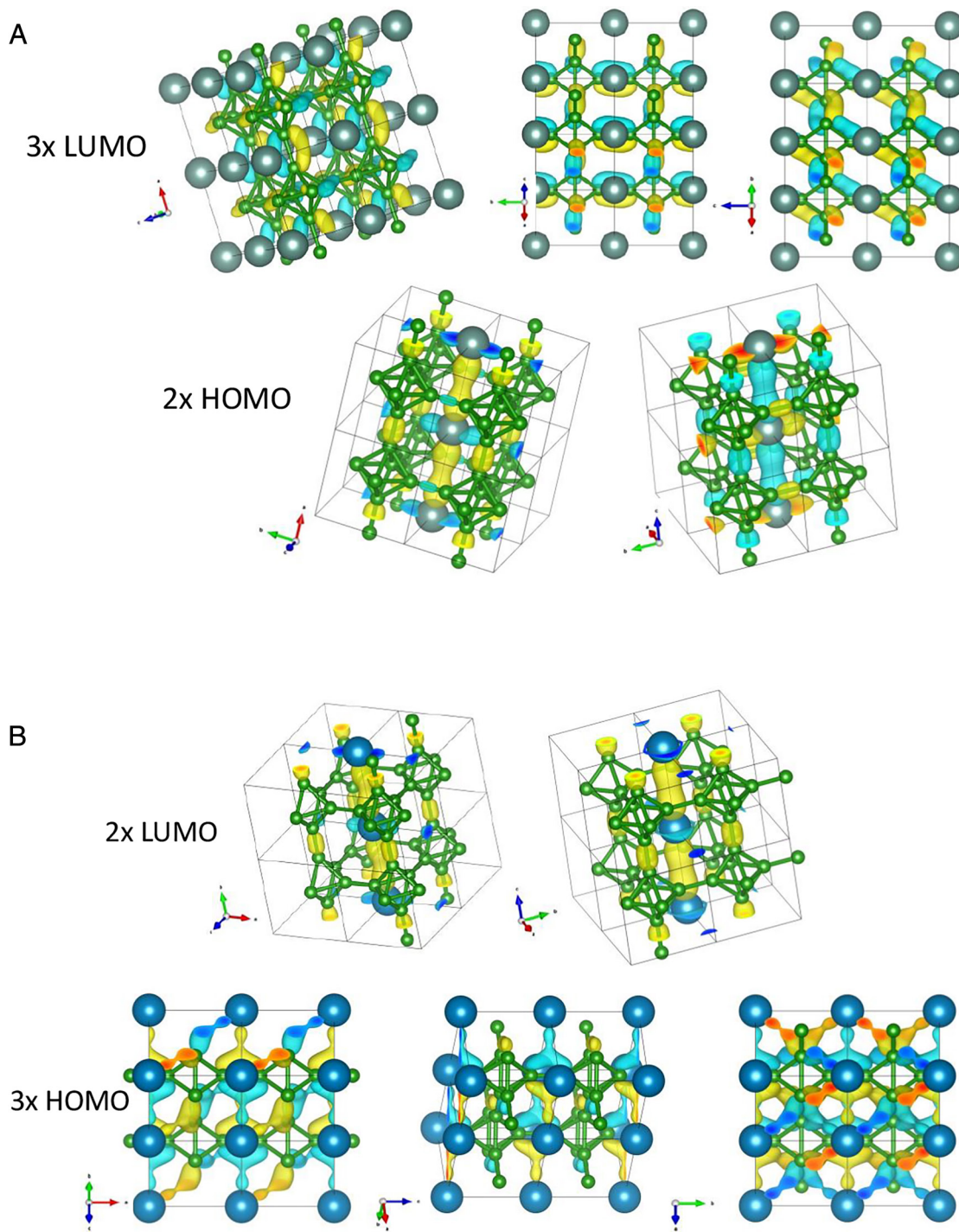


Fig. 2. Frontier orbitals of YB_6 (A) and LaB_6 (B). For each material, HOMO are shown in the *Lower* row and LUMO in the *Upper* row. Gray atoms are yttrium, blue atoms are lanthanum, and green atoms are boron. Isovalues were chosen to show the bonds reflected in the PDOS and are approximately 0.03 for σ -bonds and 0.15 for π -bonds. Due to the difference in localized σ -bonds versus delocalized π -bonds, the same isovalue could not be used for both. Lattice vectors are shown to the left of each orbital and the degeneracy is shown by 2 \times or 3 \times on the HOMO/LUMO label.

deduced that this inversion of valence and conduction bands between LaB_6 and YB_6 is due to the participation of the 4f orbitals, which are unoccupied but low-lying in lanthanum's $[\text{Xe}]5d^16s^2$ electron configuration, yet completely inaccessible in ground-state yttrium ($[\text{Kr}]4d^15s^2$).

Density of States Comparison at the Fermi Level. From the electronic band diagrams in Fig. 1 *D* and *E*, it can be clearly determined that YB_6 has a significantly larger DOS at the Fermi level than LaB_6 , making this DOS contribution to the

McMillan–Allen–Dynes (MAD) description straightforward. While only two bands comprise the Fermi surface of YB_6 , they cross E_f six times. Three bands comprise LaB_6 's Fermi surface, but all come together in degeneracy at the Γ point with two crossing E_f at only one other point and the third not at all, for a total of only three crossings of the Fermi level. All these bands have significant curvature (“band width”) at and near E_f (i.e., they are not at all flat), so their contributions to the E_f -DOS occur only due to point intersections with the Fermi level. In YB_6 , it has been established (15) that the finite states at E_f indicate metallic bonding. By contrast,

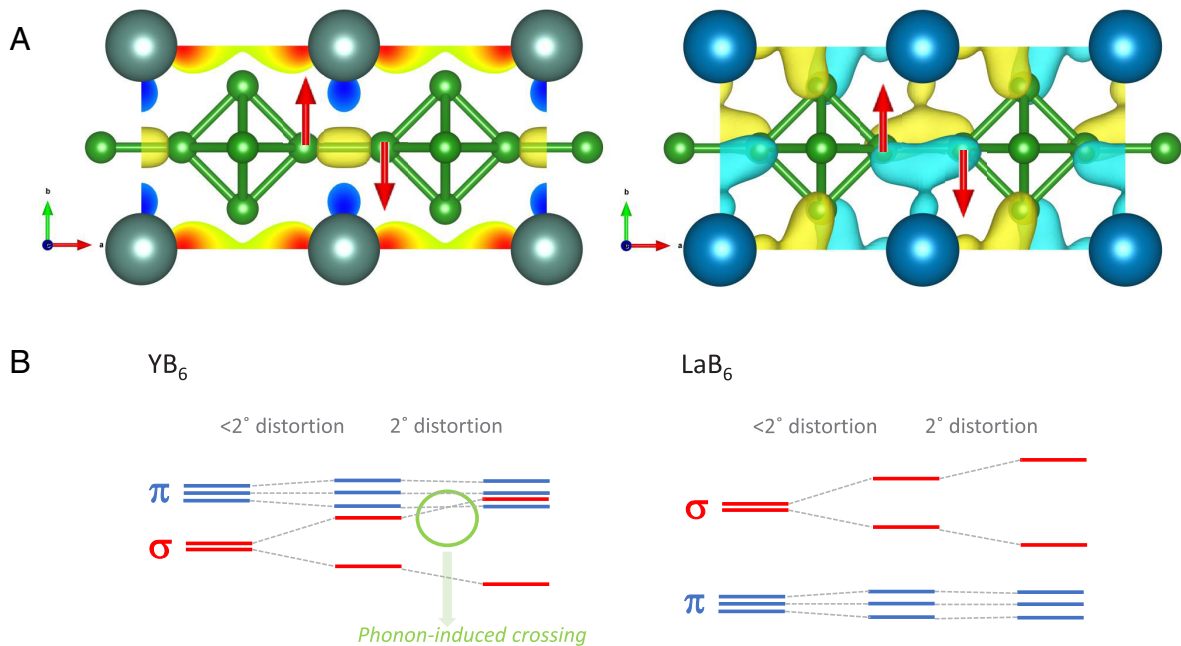


Fig. 3. (A) One of two YB_6 (Left) and LaB_6 (Right) HOMO, showing how their shapes lead to more (YB_6) or less (LaB_6) EPC. (B) Qualitative picture of orbital degeneracy breaking with the frozen phonon in YB_6 (Left) and LaB_6 (Right), noting the ZPE-accessible crossing in YB_6 .

LaB_6 exhibits essential metal–boron covalency at E_f in the π -system, contributing to a smaller E_f -DOS than that of the isolated Y–Y and B–B σ bonds we observe at the E_f of YB_6 .

Discussion

Coupling of T_{2g} Phonons to HOMO of Each Material. Now that the frontier orbitals of YB_6 and LaB_6 have been identified, we can begin to discuss how their bonding character leads to a large electron–phonon coupling, i.e., involving splitting of their degeneracies at E_f . In both materials, phonons 13 to 15 rock inter-octahedron B_2 units back and forth like a “see-saw” (Fig. 1C and GIF and interactive files for reference have been provided in *SI Appendix*). As mentioned, in YB_6 , these B_2 units are held together by a σ -bond formed by p_z -AOs, and do not engage with the metal or other B atoms at E_f . The rocking phonon is applied, the p_z orbitals go out of σ -alignment, and the σ -overlap worsens. This is shown on the *Left* of Fig. 3A.

By contrast, E_f in LaB_6 is comprised of π -bonds on B_2 units which overlap with La’s 4f orbitals at the phonon’s axis of rotation, making these bonding orbitals see-saw shaped themselves. When the B_2 unit is rocked by the phonon, the electron density between La and the center of B_2 is merely a “fulcrum” for this rocking, and the B_2 itself remains π -bonded off the bond axis with no phonon-induced misalignment of the B p_{xy} -AOs. Thus, overlap is largely unaffected by the phonon and EPC is expected to be quite low. This can be visualized on the *Right* side of Fig. 3A. Recalling that the HOMO and the phonon are triply degenerate for LaB_6 , we note that the other two phonons which do not align with the LaB_2 see-saw unit can still couple to it. Having only $\sim 2/3$ of the electron–phonon interactions per phonon, however, LaB_6 will have significantly less EPC than YB_6 , in which each component of the triply degenerate HOMO couples to all three components of the phonon. This qualitatively explains YB_6 being the superior BCS superconductor with a much higher critical temperature.

In order to assess this hypothesis rigorously, we began to examine frontier orbitals after the frozen phonons were applied and uncovered something quite striking. The mildly distorted structures resulting

from frozen phonons retain largely the shapes of their HOMO and LUMO, and unsurprisingly, degeneracies of these orbitals break according to which phonon direction couples to their overlap. At a phonon distortion of approximately 2 degrees (accessible by ZPE, as shown in *SI Appendix*, Fig. S2), however, one of the π -bands of YB_6 drops in energy, switches with one of the σ -bands, and becomes occupied at Γ (Fig. 3B). The process that occurs is, naturally, identical in all three Cartesian directions. Application of the phonon changes point group symmetry from O_h (Pm3m) to C_i , within which the π -system is of a_u symmetry, and the σ -system is a_g . Thus, the state crossing is not a conical intersection by the no-crossing theorem. Its presence, however, is nonetheless proof of major phonon-induced changes in electronic structure and indicative of strong EPC. No such crossing occurs in LaB_6 at any deformation angle computed, ZPE accessible or otherwise (*Bottom* of Fig. 3B).

Additional EPC in a Supercell. *SI Appendix*, Fig. S3 shows that in addition to the Γ point, significant EPC stems from the M point of the Brillouin zone (BZ) where all unit cells are fully out of phase with their neighbors in all three Cartesian directions. Indeed, Fig. 1 B and E show electronic band degeneracy splitting at M at the Fermi level. It is essential to understand how the mechanism of EPC present at Γ extends to the M point and does not extend to other points of high symmetry. We perform DFT calculations of $2 \times 2 \times 2$ supercells with the frozen phonon applied with the unit cell phase relations of M, X, and R and analyze the effect on the Fermi surface (FS). For the M point of interest, *SI Appendix*, Fig. S4 shows slices of the FS cut along the (001) plane at various values of k_z . Comparing YB_6 and LaB_6 , the differences are minimal, with exception of phonon 15 around $k_z = 0.4$. The changes on this slice are much larger for YB_6 .

Fig. 4 A and B show the unperturbed Fermi surface of YB_6 (no supercell) for two values of k_z . The red curves show the band folding of these slices into a $2 \times 2 \times 1$ supercell (for the sake of simplicity, the folding along k_z is ignored). The folded BZ is the dashed box. The folding induces new degeneracies, or Fermi nesting, on the folded BZ. These points and their position in the original BZ are marked by green points, which an arrow going from Γ to M connects in the original BZ.

This arrow's direction coincides with the phonon with the largest EPC, causing a sizable Fermi nesting. Fig. 4C shows the actual FS of a $2 \times 2 \times 2$ supercell of YB_6 , with $k'_z = 0.4$ (in the folded BZ). Again, the bands of interest are in red. The other bands come from the folding along k_z and are of no interest here. Fig. 4D shows the previous FS of Fig. 4C, but under the effect of frozen phonon 15 with modest amplitude. We readily see that these new degeneracies introduced by the supercell band folding are broken by the phonon. By symmetry, the same phenomenon occurs for phonons 13 and 14, along the (100) and (010) planes, respectively.

To address why this nesting implies a large EPC specifically at (and near) the M point, and why it is more drastic in YB_6 than in LaB_6 , we consider the phonon's effect on the boron octahedral cage around the metals in each supercell. At X and R, the application of the frozen phonon breaks lattice O_h symmetry, but each metal atom has the same surrounding boron geometry (Fig. 5A, noting that the unit cells are related by inversion symmetry at X but still give the same surroundings of the metal). At the M point, however, two different sizes of the boron cage are introduced with the phonon, emphasized with black squares, giving the lattice twice the periodicity as at equilibrium before. This effect, known as a dimerization, is well studied in other, quasi-1-dimensional (1-D) materials in the context of Peierls distortions (56, 57), which cause periodic fluctuations in electron density known as charge density waves (CDW) (58).

The Peierls mechanism involves the splitting of a degeneracy in a metallic system, lowering its energy at the same time the distortion increases the energy. In 1-D systems, this mechanism is energetically favorable for a finite distortion. But, in general, it is not the case for 3D crystals such as YB_6 and LaB_6 . Nevertheless, a Peierls-like distortion or dimerization is very effective for lifting a degeneracy in a quasi-1D band, and a large EPC is expected from it.

Note S1 gives a full explanation of a tight binding (TB) model in the context of YB_6 and LaB_6 , but what is most important when comparing the two materials is the "1D-ness" of their valence bands. It is straightforward to identify a quasi-1-D chain in YB_6 as the Y-Y σ bonds run parallel to the prominent B-B σ -bonds (Fig. 5b). When the phonon acts at M, Y atoms obtain twice the period in this chain direction and a splitting of degeneracies should appear, explaining the large changes obtained by the frozen phonon 15 in *SI Appendix*, Fig. S4. On the other hand, the most 1-D-like periodicity of LaB_6 's HOMO is a 45° lattice rotation from that of YB_6 's and the boron octahedra become part of the "chain." This makes the band "less 1-D," and a dimerization in LaB_6 should not be as effective as in YB_6 to split degeneracies. In the context of the TB model, the La atoms and the octahedra will have very different on-site terms, leaving just one TB band close to the Fermi level. This band in LaB_6 experiences a weaker Peierls-like effect since the other dimensions are unaffected by the dimerization (indeed, there is still nonzero EPC at M), but YB_6

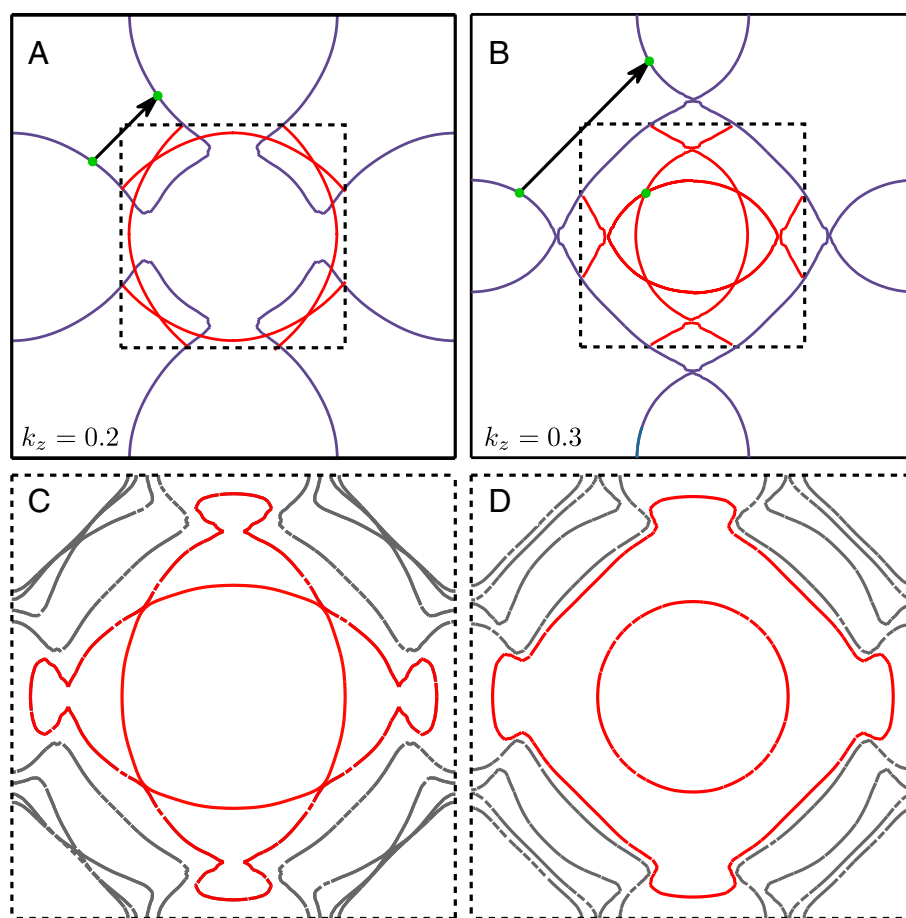


Fig. 4. (A) Equilibrium YB_6 FS at $k_z = 0.2$. Blue lines show the unit cell FS slice, solid black lines show the (001) plane of the unit cell BZ, dotted black lines show the (001) plane of a $2 \times 2 \times 1$ supercell BZ. Green points denote sites where Fermi nesting occurs with the band folding. An arrow denotes the direction of the path between Γ and M. Bands of interest due to nesting in the (001) plane are in red. (B) Equilibrium YB_6 FS at $k_z = 0.3$, using the same symbols and coloring as (A). (C) FS at $k_z = 0.4$ of a $2 \times 2 \times 2$ supercell at equilibrium. (D) FS at $k_z = 0.4$ of a $2 \times 2 \times 2$ supercell with frozen phonon 15 applied, showing that the red bands of interest now have broken degeneracies. The extra bands in gray are due to the folding in k_z .

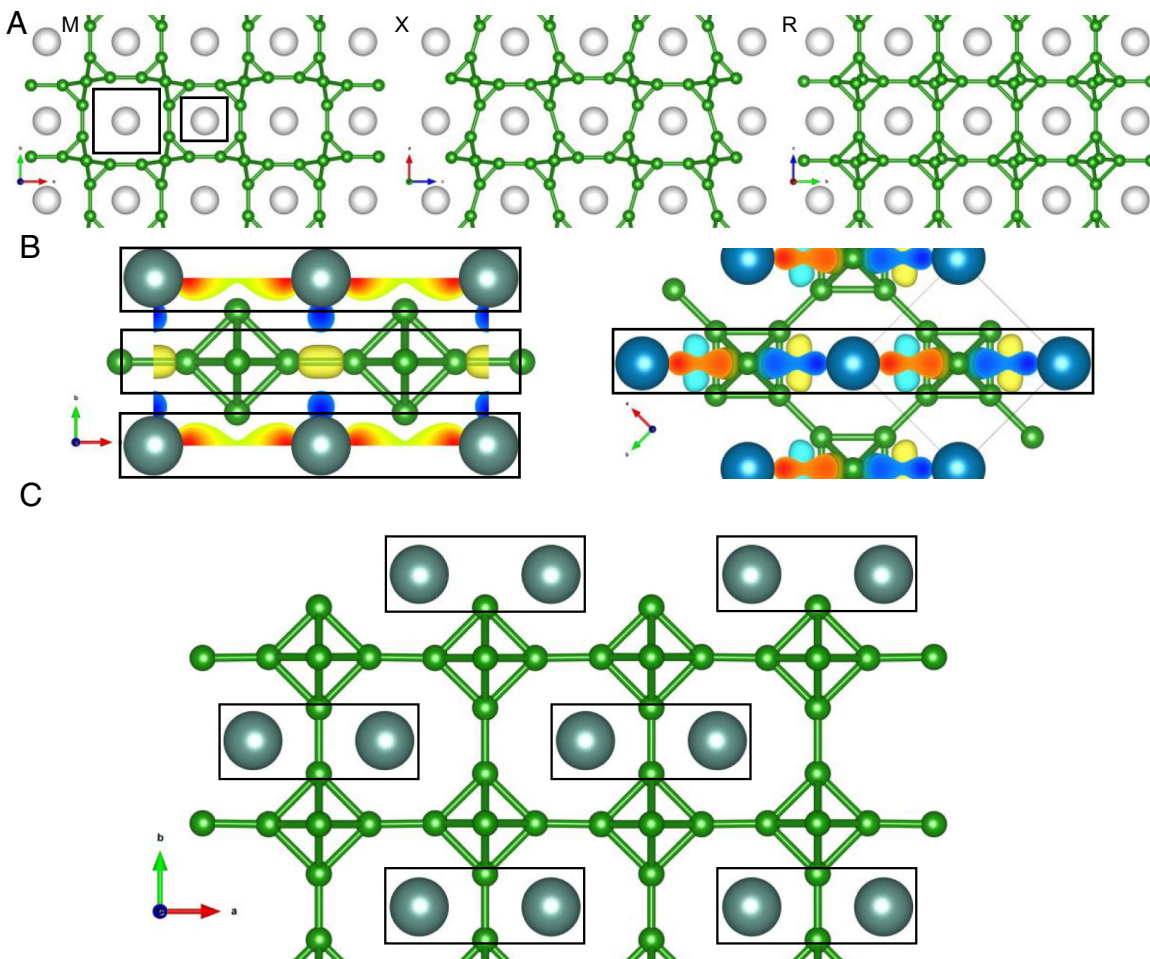


Fig. 5. (A) Frozen phonon applied to the supercell at the M (Left), X (Middle), and R (Right) points. White atoms can be either Y or La. Green atoms are boron. Black squares emphasize the difference in surroundings of the metal at the M point. (B) 1-D “chains” formable by the valence bands of YB_6 (Left) and LaB_6 (Right). Chains are noted with black rectangles. Y atoms are gray, La atoms are blue, and B atoms are green. (C) Dimerization of the YB_6 lattice under a softened phonon, with dimers boxed in black. Comparison to (B) shows this occurs in the same direction of one of the Y–Y σ -bonds, creating EPC in the form of a Peierls-like effect. Y atoms are gray, and B atoms are green.

is decidedly the “more 1-D” of the two materials, explaining the higher EPC and T_c .

While some experimental studies predict EPC of acoustic phonons to be low in both these materials (48), others attribute a great deal of YB_6 's higher T_c to these phonons (22). Phonons with very low frequency are likely to be highly anharmonic, so the approximations used in EPC calculations (*SI Appendix, Fig. S3*) are unlikely to provide useful information. Thus, we rely only on frozen phonon calculations here. It can be readily seen from Fig. 1 A and B that the three lowest of these phonons soften for YB_6 , but not LaB_6 . Thus, for YB_6 , a small perturbation (changes in temperature, pressure, etc.) can turn the frequency of the acoustic phonons negative, triggering a change of equilibrium geometry. This difference in phonon spectrum has been attributed to the slightly larger atomic radius of lanthanum leaving less space in the boron cage for the metal atom to “rattle” along the acoustic phonon modes (45).

Indeed, we observe large changes in the Fermi surface for YB_6 due to two of the frozen acoustic phonons at M (phonons 2 and 3), but little to no observable change for LaB_6 (*SI Appendix, Fig. S4*). Once again, this is readily explained by bonding at E_f . In the case of YB_6 , a totally symmetric mode at the Γ point will not affect the d–d bonding of Y atoms, but within other supercells, σ overlap will be strongly affected by movement of Y out of phase

between unit cells, much like the rocking modes 13 to 15 affecting σ -overlap between boron atoms. LaB_6 , however, has no such metal–metal bonding, so no such EPC arises from the acoustic phonons. The vast majority of the LaB_6 electron density at E_f is on the unaffected boron octahedra for LaB_6 , and thus EPC is low.

From another viewpoint, phonon softening is a main signature of a Peierls distortion (56), and we thus consider these two acoustic phonons in the context of dimerization. Fig. 5C shows the resulting geometry when one of the two frozen phonons is applied, and along only one axis (the same axis a Y–Y σ bond runs along), a clear dimerization occurs between the Y atoms. The other frozen phonon gives the same result, but along a different axis with the other σ bond. The third acoustic phonon, which further dips at M and along the Γ –R path, acts along the final axis, which has no σ bonding. Indeed, Lortz et al find a large EPC peak for YB_6 at 8 meV but a much smaller one at 4.5 eV (22), in good agreement with the computed frequencies at M: 7 meV for phonons 2 and 3 and 3.6 meV for phonon 1.

Given that the Y atoms are σ -bonded along a single direction per Bloch state at E_f , the effect of the acoustic phonons is much closer to the “textbook” example of a 1-D chain of hydrogen atoms than the previous Peierls argument of phonons 13 to 15. Though competition of other relevant phonons in a 3-D lattice prevents an actual CDW, this dynamical Peierls effect is more “traditional”

than that of phonons 13 to 15 in that the tight-binding hopping strength is modified, rather than the on-site energy. This is again discussed in detail in *SI Appendix, Note S1*. In summary, we observe two ways to induce a Peierls-like distortion in YB_6 , from low-energy and high-energy phonons.

Effects of Isotropic Pressure and Stretching. The effects of strain and pressure are essential in studying bonding-governed properties of materials (59–61): hexaborides (7, 62–66) or otherwise. Specifically in the case of hexaboride superconductors, the effects of isotropic pressure have been thoroughly studied experimentally and computationally (36, 42, 43, 48), including in the context of phase transitions out of the $\text{Pm}\bar{3}\text{m}$ space group (39, 41). Experimentally, pressure has been shown to lower the superconducting transition of YB_6 (43), and this has been attributed to hardening of the lowest-energy, acoustic phonon modes, a “rattling” of Y in the boron cage which Xu et al. computationally deem responsible for superconductivity (45). Our calculations of k-point and band-resolved phonon linewidths and frozen phonons’ effects on electronic band structure, however, show these phonons to contribute only partially to EPC, along with phonons 13 to 15 and 19 to 21 involving the bridging boron atoms between octahedra.

As shown in Fig. 6, we find that computed band structures with applied pressure slightly expand the gap between valence and conduction bands, though both materials remain metals. We compute pressures up to 112 kbar in order to match experiment (43). Though phonon dispersion and EPC calculations at a variety of pressures are computationally prohibitive, the same argument of phonon hardening/constriction with compression can be made qualitatively. The widening of the energy difference between valence and conduction bands has to do with the change in AO-overlap upon compression: antibonding states will always rise in energy, and the bonding states may rise or drop, depending on the bond length imposed by the lattice, compared to the optimum for the given pair of atoms (60). The shifts are more pronounced for the σ -bonds, i.e., HOMO of YB_6 and LUMO of LaB_6 , than for π -bonds that have weaker AO-overlaps. These shifts in band energies will affect the extent to which phonons 13 to 15 and 19 to 21 can interact with them (60). This is a question for future study.

Particularly for the case of LaB_6 , where localized f-orbitals are the cause of its deviation from YB_6 , the question is begged whether stretching these materials isotropically could have the opposite effect of applied pressure: increasing T_c . If the boron π system becomes so far removed from La that the 4f interaction can no

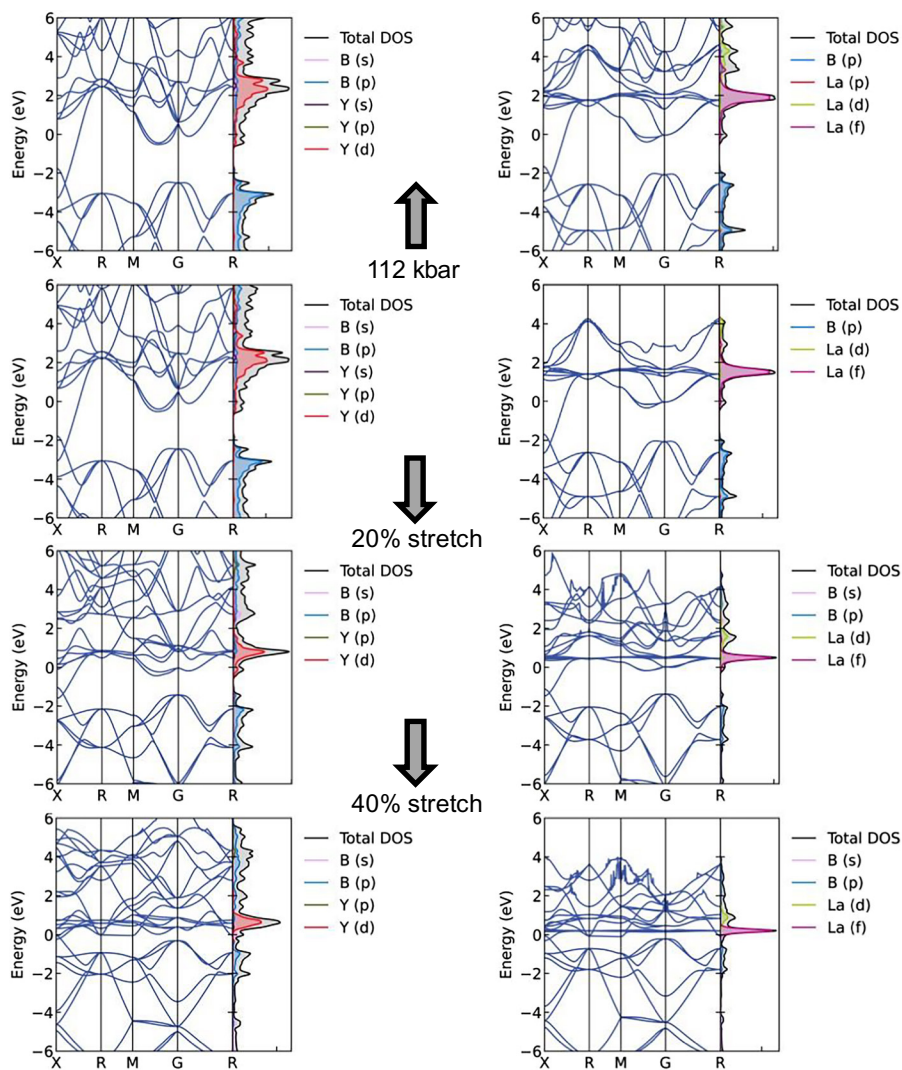


Fig. 6. Effects of pressure and isotropic stretching on the electronic band structures of YB_6 (Left) and LaB_6 (Right). The percent stretching indicates that each of the three lattice vectors was stretched by the given percentage.

longer stabilize it, the valence and conduction bands could theoretically swap in energy order and a band structure similar to YB_6 could be observed. As demonstrated in Fig. 6, the equilibrium valence and conduction bands can be made degenerate in LaB_6 but never to flip. As before, this effect is less pronounced in the π bands than the σ bands. Furthermore, this degeneracy occurs at extreme bond stretching lengths (1.4 times the equilibrium lattice vector of 4.155 Å for LaB_6 and 4.098 Å for YB_6) at which, in reality, the material would almost certainly experience mechanical failure. For context, based on their thermal expansion coefficients, a bond stretch of 1.6% length corresponds to a heating of approximately 2,000 °C (67). Furthermore, static electron correlation dramatically increases at stretched bond lengths near and past the Coulson-Fischer point, which can make DFT predictions incorrect. The question of whether anisotropic expansion of the lattice, by chemical doping or mechanical stress, can produce this desired effect in LaB_6 may be addressed in a future study.

Conclusions. Lanthanum and yttrium hexaboride have been shown in this study to superconduct by different electron–phonon coupling mechanisms as governed by their chemical bonding and the phonons we show responsible for superconductivity. LaB_6 , a relatively unextraordinary superconductor at $T_c = 0.45$ K, has a Fermi level (E_F) comprised of B–B π bonds overlapping with 4f orbitals of La. This see-saw shaped bonding of the HOMO aligns with the B_2 rocking motion of the main, triply degenerate phonon responsible for superconductivity, leading to less electron–phonon coupling. YB_6 , the second-highest T_c superconductor of the metal borides at 8.4 K, is remarkably different from its La counterpart. Due to the unavailability of f orbitals for bonding stabilization, the B–B π system is unoccupied in YB_6 and E_F is instead made up of σ bonds. The directionality of this bonding makes it couple to the lattice much more strongly than the π system and an accessible crossing of states is even accessible by the phonons, an indicator of strong EPC which is not present at all in LaB_6 . Softened, acoustic phonons also play a role in the YB_6 EPC due to coupling to Y–Y σ bonds, which have no such effect in LaB_6 . Finally, we show the effects of isotropic pressure and stretching on the electronic structure of these materials as it corresponds to their superconducting nature. This bonding and molecular orbital–based assessment of superconductivity paves a path for future characterization, design, and prediction of potential superconductors which is logical and accessible to any chemist.

Materials and Methods

Computational Methods. DFT calculations were performed using the Vienna Ab-initio Software Package (VASP) (68, 69). Due to its excellent agreement with positron annihilation spectroscopy experiment in terms of the Fermi surface (40), the versatile PW91 exchange–correlation functional (70, 71), of the generalized gradient approximation (GGA) family of functionals, was used without any Hubbard U correction on d or f orbitals. Additionally, the calculated band structure of LaB_6 is in excellent agreement with the electronic band measured by angle-resolved photoelectron spectroscopy (ARPES) (37). Furthermore, study of YB_6 via photoelectron spectroscopy shows agreement with our computed DOS and the bonding picture we describe at the Fermi level (72).

Use of a van-der-Waals correction via the PBE-D3 formalism (D3 damping parameters for PW91 are not yet available) was found to have no effect on band structures or energy differences, additionally showing expected matching between the PW91 and PBE GGA functionals. Despite the fact that LaB_6 and YB_6 are metals and expected to be highly delocalized, the possible localization of 4f electrons in LaB_6 was assessed through use of a 5 eV Hubbard U correction (73) on these orbitals applied in the rotationally invariant scheme of Dudarev et al. (74). This correction was found to change band shape (SI Appendix, Fig. S5) but

not the atomic orbital character of the frontier orbitals of LaB_6 or its phonon dispersion. Unit cells, in good agreement with experimental lattice constants, were obtained from the Materials Project database (75) and their atoms' geometries were optimized in VASP to minimize forces (details below).

All DFT calculations were initially performed with the inclusion of self-consistent spin-orbit coupling (SOC) within the PAW sphere, but this was found to have no effect on the properties of interest in this study: Kohn-Sham orbital shape (assessed via real space projection of large and small spinor components), unit cell geometry and dimension, density of states (DOS), and band topology (including with the frozen phonon and its induced crossing of states in YB_6). Specifically for DOS and band topology, no bands were inverted due to the addition of SOC, nor were relevant band degeneracies broken (SI Appendix, Fig. S6). Scalar relativistic effects remain included within the projector-augmented wave (PAW) (76) pseudopotentials of VASP. All DFT calculations were spin-unrestricted, but with the exception of extreme bond stretching at which static correlation increases and DFT begins to break down, spin-up and spin-down components were always identical. A plane-wave kinetic energy cutoff of 600 eV was used, and PAW charge densities were mixed up to angular momentum quantum number 6. Electronic energy self-consistency was enforced up to 10^{-6} eV, and all-force-norm self-consistency in geometry optimization was enforced up to 10^{-5} eV/Å.

Unfortunately, any changes in band structure due to post-DFT electron correlation (band renormalization) proved too computationally expensive to compute within the G_0W_0 approximation, which does not require choice of Hubbard parameters as in DFT+U. Electron correlation has been shown to be crucial to properties of localized, nonconducting metal hexaborides deeper in the 4f block (6, 9), but can be considered negligible for the itinerant electronic structure of YB_6 and LaB_6 . This is also consistent with our benchmarking showing no need for a van-der-Waals correction and the minimal effects of localizing 4f orbitals with a Hubbard correction.

With the exception of density functional perturbation theory (DFPT) calculations requiring a 3x3x3 supercell for phonon spectra, VASP calculations were all performed using a mesh of $21 \times 21 \times 21$ k-points using the Monkhorst-Pack scheme. This number of k-points was required for geometry optimization to ensure no presence of imaginary phonons. For DFPT calculations, the supercell size permitted 1/3 the k-points in each direction, i.e., $7 \times 7 \times 7$. Fermi smearing of small width, 0.05 eV, was used in all calculations, with energies taken in the limit of zero smearing. Band structure calculations were performed with additional grid support (ADDGRID=T), and densities of states (DOS) were evaluated on 4,000 grid points. Pressure was applied to unit cells via the PSTRESS tag in VASP (minding units), and unit cells were stretched with scaled atomic distances using the Atomic Simulation Environment (77, 78).

Band and k-point resolved electron–phonon coupling magnitudes, directly proportional to phonon linewidths (taken at the fourth smearing number), were computed using Quantum Espresso (79, 80) via the same DFT parameters as in VASP and overlaid onto phonon dispersion plots. A tutorial for this procedure can be found here: <https://gitlab.com/QEF/q-e/-/tree/develop/PHonon/examples/example03>. Phonon modes were determined using the Phonopy software (81, 82) and visualized using phononwebsite (<https://henriquemiranda.github.io/phononwebsite/phonon.html>). Kohn-Sham molecular orbitals and spinors (in the case of SOC benchmarking) were plotted using the WAVECARplot (83, 84) and WaveTransPlot (85) scripts and visualized using VESTA (86–88). Phonon modes were added to VESTA-visualized unit cell files using the VaspVib2XSF script (<https://github.com/QijingZheng/VaspVib2XSF>). Electronic and phonon bands, including projected densities of states (PDOS), were plotted using the SUMO code (89).

Data, Materials, and Software Availability. Vibrational mode visualization files for the phonon bands of YB_6 and LaB_6 data can be visualized after changing extension from .txt to .yaml at phononwebsite (<https://henriquemiranda.github.io/phononwebsite/phonon.html>) (90). All other data are included in the manuscript and/or supporting information.

ACKNOWLEDGMENTS. R.H.L. performed the calculations on Department of Energy (DOE) National Energy Research Scientific Computing Center supercomputers under contract no. DE-AC02-05CH11231 and acknowledges support by the NSF Graduate Research Fellowship under Grant No. DGE-2034835.

An additional award of computer time was provided by the Innovative and Novel Computational Impact on Theory and Experiment program. This research used resources of the Argonne Leadership Computing Facility, which is a DOE Office of Science User Facility supported under contract DE-AC02-06CH11357. J.M. acknowledges the Spanish "Ministerio de Ciencia e Innovación" (NSF number PID2021-122763NB-I00). C.E.D. acknowledges support by the NSF Graduate Research Fellowship under Grant No. DGE-2034835. F.M. acknowledges Fondo

Nacional de Desarrollo Científico y Tecnológico projects 1231487, 1220715 and by the Center for the Development of Nanosciences and Nanotechnology, CEDENNA AFB 220001. F.M. is supported by Conicyt PIA/Anillo ACT192023. Powered@The National Laboratory for High Performance Computing. This research was partially supported by the supercomputing infrastructure of the NLHPC (ECM-02). A.N.A. acknowledges Brown Science Foundation Award 1168. R.H.L. thanks Ashley Parkhurst for artistic feedback on figures.

1. R. W. Johnson, A. H. Daane, Electron requirements of bonds in metal borides. *J. Chem. Phys.* **38**, 425–432 (1963).
2. L. Zhu, G. M. Borstad, R. E. Cohen, T. A. Strobel, Pressure-induced polymorphism in SrB₆ and deformation mechanisms of covalent networks. *Phys. Rev. B* **100**, 214102 (2019).
3. H. C. Longuet Higgins, M. D. V. Roberts, The electronic structure of the borides MB₆. *Proc. R. Soc. Lond. A Math. Phys. Sci.* **224**, 1158 (1954).
4. J. Kuneš, W. E. Pickett, Kondo and anti-Kondo coupling to local moments in EuB₆. *Phys. Rev. B* **69**, 165111 (2004).
5. G. Li *et al.*, Two-dimensional Fermi surfaces in Kondo insulator SmB₆. *Science* **346**, 1208–1212 (2014).
6. P. J. Robinson *et al.*, Dynamical bonding driving mixed valency in a metal boride. *Angew. Chem. Int. Ed.* **59**, 10996–110022 (2020).
7. G. E. Grechnev, A. V. Logosha, A. S. Panfilov, N. Y. Shitsevalova, Pressure effects on magnetic properties and electronic structure of EuB₆ and GdB₆. *J. Alloys Compd.* **511**, 5–8 (2012).
8. I. Popov, N. Baadjji, S. Sanvito, Magnetism and antiferroelectricity in MgB₆. *Phys. Rev. Lett.* **108**, 107205 (2012).
9. J. Munarriz, P. J. Robinson, A. N. Alexandrova, Towards a single chemical model for understanding lanthanide hexaborides. *Angew. Chem. Int. Ed.* **59**, 22684–22689 (2020).
10. L. Sun, Q. Wu, Pressure-induced exotic states in rare earth hexaborides. *Rep. Progr. Phys.* **79**, 084503 (2016).
11. J. T. Cahill, O. A. Graeve, Hexaborides: A review of structure, synthesis and processing. *J. Mater. Res. Technol.* **8**, 6321–6335 (2019).
12. L. Xiao *et al.*, Study on the electronic structure and the optical performance of YB₆ by the first-principles calculations. *AIP Adv.* **1**, 022140 (2011).
13. H. Kasai, E. Nishibori, Spatial distribution of electrons near the Fermi level in the metallic LaB₆ through accurate X-ray charge density study. *Sci. Rep.* **7**, 41375 (2017).
14. Y. Zhou, F. Dai, H. Xiang, B. Liu, Z. Feng, Shear anisotropy: Tuning high temperature metal hexaborides from soft to extremely hard. *J. Mater. Sci. Technol.* **33**, 1371–1377 (2017).
15. Y. C. Zhou, B. Liu, H. M. Xiang, Z. H. Feng, Z. P. Li, YB₆: A 'ductile' and soft ceramic with strong heterogeneous chemical bonding for ultrahigh-temperature applications. *Mater. Res. Lett.* **3**, 210–215 (2015).
16. G. Schell, H. Winter, H. Rietschel, F. Gompf, Electronic structure and superconductivity in metal hexaborides. *Phys. Rev. B* **25**, 1589 (1982).
17. Z. Fisk, P. H. Schmidt, L. D. Longinotti, Growth of YB₆ single crystals. *Mater. Res. Bull.* **11**, 1019–1022 (1976).
18. P. Szabó *et al.*, Superconducting energy gap of YB₆ studied by point-contact spectroscopy. *Physica C* **460–462**, 626–627 (2007).
19. B. T. Matthias *et al.*, Superconductivity and antiferromagnetism in boron-rich lattices. *Science* **159**, 530 (1968).
20. O. M. Vyaselev *et al.*, Electron spin dynamics in a hexaboride superconductor YB₆ probed by 89Y and 11B NMR. *J. Alloys Compd.* **921**, 165627 (2022).
21. Z. Fisk, Superconducting borides. *AIP Conf. Proc.* **231**, 155–164 (1991). <https://doi.org/10.1063/1.40864>.
22. R. Lortz *et al.*, Superconductivity mediated by a soft phonon mode: Specific heat, resistivity, thermal expansion, and magnetization of YB₆. *Phys. Rev. B* **73**, 024512 (2006).
23. V. Moshchalkov *et al.*, Type-1.5 superconductivity. *Phys. Rev. Lett.* **102**, 117001 (2009).
24. D. C. Larbaestier *et al.*, Strongly linked current flow in polycrystalline forms of the superconductor MgB₂. *Nature* **410**, 186–189 (2001).
25. J. Nagamatsu, N. Nakagawa, T. Muranaka, Y. Zenitani, J. Akimitsu, Superconductivity at 39 K in magnesium diboride. *Nature* **410**, 63–64 (2001).
26. H. Zhai, F. Munoz, A. N. Alexandrova, Strain to alter the covalency and superconductivity in transition metal diborides. *J. Mater. Chem. C, Mater.* **7**, 10700–10707 (2019).
27. S. Singh *et al.*, High-temperature phonon-mediated superconductivity in monolayer Mg₂B₂C₂. *npj Quant. Mater.* **7**, 37 (2022).
28. T. T. Pham, D. L. Nguyen, First-principles prediction of superconductivity in MgB₃C₃. *Phys. Rev. B* **107**, 134502 (2023).
29. A. B. Migdal, Interaction between electrons and lattice vibrations in a normal metal. *JETP* **34**, 996–1001 (1958).
30. G. M. Eliashberg, Interactions between electrons and lattice vibrations in a superconductor. *Sov. Phys. JETP-USSR* **11**, 696–702 (1960).
31. W. L. McMillan, Transition temperature of strong-coupled superconductors. *Phys. Rev.* **167**, 331–344 (1968).
32. P. B. Allen, R. C. Dynes, Transition temperature of strong-coupled superconductors reanalyzed. *Phys. Rev. B* **12**, 905 (1975).
33. M. I. Tsindilekht *et al.*, Linear and nonlinear low-frequency electrostatics of surface superconducting states in an yttrium hexaboride single crystal. *Phys. Rev. B* **78**, 024522 (2008).
34. P. Szabó, P. Samuely, J. Gironovsky, T. Mori, Strong coupling features in the point-contact spectra of the YB₆ superconductor. *J. Phys. Conf. Ser.* **150**, 052253 (2009).
35. Y. S. Ponomov, A. A. Makhnev, S. V. Streltsov, V. B. Filippov, N. Y. Shitsevalova, Electronic Raman scattering and the electron-phonon interaction in YB₆. *JETP Lett.* **102**, 503–507 (2015).
36. M. Romero *et al.*, Ab initio calculations of the elastic, vibrational, electronic properties, and electron-phonon constant of superconducting YB₆ compound under low pressure. *Phys. Scr.* **96**, 125850 (2021).
37. A. Rattanachata *et al.*, Bulk electronic structure of lanthanum hexaboride (LaB₆) by hard X-ray angle-resolved photoelectron spectroscopy. *Phys. Rev. Mater.* **5**, 055002 (2021).
38. J. A. Alarco, P. C. Talbot, I. D. R. Mackinnon, Comparison of functionals for metal hexaboride band structure calculations. *Model. Numer. Simul. Mater. Sci.* **04**, 53–69 (2014).
39. P. Teredesai *et al.*, High pressure phase transition in metallic LaB₆: Raman and X-ray diffraction studies. *Solid State Commun.* **129**, 791–796 (2004).
40. J. Ketels *et al.*, Fermi surface modeling of light-rare-earth hexaborides using positron annihilation spectroscopy. *Phys. Status Solidi B, Basic Res.* **259**, 2100151 (2022).
41. J. Wang *et al.*, High-pressure evolution of unexpected chemical bonding and promising superconducting properties of YB₆. *J. Phys. Chem. C* **122**, 27820–27828 (2018).
42. R. Khasanov *et al.*, Effect of pressure on the Ginzburg-Landau parameter $\kappa = \lambda/\xi$ in YB₆. *Phys. Rev. Lett.* **97**, 157002 (2006).
43. S. Gabáni *et al.*, High-pressure effect on the superconductivity of YB₆. *Phys. Rev. B* **90**, 045136 (2014).
44. J. A. Alarco, M. Shahbazi, P. C. Talbot, I. D. R. Mackinnon, Spectroscopy of metal hexaborides: Phonon dispersion models. *J. Raman Spectrosc.* **49**, 1985–1998 (2018).
45. Y. Xu *et al.*, First-principles study of the lattice dynamics, thermodynamic properties and electron-phonon coupling of YB₆. *Phys. Rev. B* **76**, 214103 (2007).
46. N. Sluchanko *et al.*, Lattice instability and enhancement of superconductivity in YB₆. *Phys. Rev. B* **96**, 144501 (2017).
47. P. Szabó *et al.*, Point-contact spectroscopy of the phononic mechanism of superconductivity in YB₆. *Supercond. Sci. Technol.* **26**, 045019 (2013).
48. Y. S. Ponomov, N. Y. Shitsevalova, Phonons in YB₆ and LaB₆: Effects of temperature and pressure. *JETP Lett.* **102**, 295–300 (2015).
49. H. J. Choi, D. Roundy, H. Sun, M. L. Cohen, S. G. Louie, The origin of the anomalous superconducting properties of MgB₂. *Nature* **418**, 758–760 (2002).
50. H. W. T. Morgan, A. N. Alexandrova, Electron counting and high-pressure phase transformations in metal hexaborides. *Inorg. Chem.* **61**, 18701–18709 (2022).
51. J. Bardeen, L. N. Cooper, J. R. Schrieffer, Theory of superconductivity. *Phys. Rev.* **108**, 1175 (1957).
52. P. J. Robinson, X. Zhang, T. McQueen, K. H. Bowen, A. N. Alexandrova, SmB₆-cluster anion: Covalency involving f orbitals. *J. Phys. Chem. A* **121**, 1849–1854 (2017).
53. H. Liu, I. I. Naumov, R. Hoffmann, N. W. Ashcroft, R. J. Hemley, Potential high-Tc superconducting lanthanum and yttrium hydrides at high pressure. *Proc. Natl. Acad. Sci. U.S.A.* **114**, 6990–6995 (2017).
54. S. Adhikari, P. Mukhopadhyay, Physical metallurgy of beryllium and its alloys. *Miner. Process. Extr. Metall. Rev.* **14**, 253–299 (1995).
55. S. Maintz, V. L. Deringer, A. L. Tchougréeff, R. Dronskowski, LOBSTER: A tool to extract chemical bonding from plane-wave based DFT. *J. Comput. Chem.* **37**, 1030–1035 (2016).
56. R. Peierls, *More surprises in theoretical physics* (Princeton University Press, Princeton, NJ, 1991). <https://doi.org/10.2307/j.ctv10crg2s>.
57. P. W. Anderson, P. A. Lee, M. Saitoh, Remarks on giant conductivity in TTF-TCNQ. *Solid State Commun.* **13**, 595–598 (1973).
58. R. E. Thorne, Charge-density-wave conductors. *Phys. Today* **49**, 42–47 (1996).
59. K. P. Hilleke, T. Bi, E. Zurek, Materials under high pressure: A chemical perspective. *Appl. Phys. A, Mater. Sci. Process.* **128**, 441 (2022).
60. P. J. Robinson, A. N. Alexandrova, Assessing the bonding properties of individual molecular orbitals. *J. Phys. Chem. A* **119**, 12862–12867 (2015).
61. J. Lei *et al.*, Understanding how bonding controls strength anisotropy in hard materials by comparing the high-pressure behavior of orthorhombic and tetragonal tungsten monoboride. *J. Phys. Chem. C* **122**, 5647–5656 (2018).
62. Y. Zhou *et al.*, Pressure-induced quantum phase transitions in a YbB₆ single crystal. *Phys. Rev. B* **92**, 241118 (2015).
63. G. Weill, I. A. Smirnov, V. N. Gurin, Electrical transport properties of EuB₆ under pressure. New experimental data. *Phys. Status Solidi A* **53**, 119–123 (1979).
64. T. Sakai, G. Oomi, Y. Uwatoko, S. Kunii, Effect of pressure on the metamagnetic transition of DyB₆ single crystal. *J. Magn. Magn. Mater.* **310**, 1732–1734 (2007).
65. N. P. Butch *et al.*, Pressure-resistant intermediate valence in the kondo insulator SmB₆. *Phys. Rev. Lett.* **116**, 156401 (2016).
66. A. Stern, M. Dzero, V. M. Galitski, Z. Fisk, J. Xia, Surface-dominated conduction up to 240 K in the Kondo insulator SmB₆ under strain. *Nat. Mater.* **16**, 708–711 (2017).
67. C. H. Chen, T. Aizawa, N. Iyi, A. Sato, S. Otani, Structural refinement and thermal expansion of hexaborides. *J. Alloys Compd.* **366**, 6–8 (2004).
68. G. Kresse, J. Hafner, Ab initio molecular dynamics for liquid metals. *Phys. Rev. B* **47**, 558 (1993).
69. G. Kresse, J. Furthmüller, Efficient iterative schemes for ab initio total-energy calculations using a plane-wave basis set. *Phys. Rev. B* **54**, 11169 (1996).
70. J. P. Perdew, Y. Wang, Accurate and simple analytic representation of the electron-gas correlation energy. *Phys. Rev. B* **45**, 13244 (1992).
71. J. P. Perdew *et al.*, Atoms, molecules, solids, and surfaces: Applications of the generalized gradient approximation for exchange and correlation. *Phys. Rev. B* **46**, 6671 (1992).
72. S. Souma *et al.*, Direct observation of superconducting gap in YB₆ by ultrahigh-resolution photoemission spectroscopy. *J. Electron. Spectrosc. Relat. Phenom.* **144–147**, 503–506 (2005).
73. W. L. Li, C. Ertural, D. Bogdanovski, J. Li, R. Dronskowski, Chemical bonding of crystalline LnB₆ (Ln = La-Lu) and its relationship with Ln₂B₂ gas-phase complexes. *Inorg. Chem.* **57**, 12999–13008 (2018).
74. S. Dudarev, G. Botton, Electron-energy-loss spectra and the structural stability of nickel oxide: An LSDA+U study. *Phys. Rev. B* **57**, 1505 (1998).
75. A. Jain *et al.*, Commentary: The materials project: A materials genome approach to accelerating materials innovation. *APL Mater.* **1**, 011002 (2013).
76. P. E. Blöchl, Projector augmented-wave method. *Phys. Rev. B* **50**, 17953 (1994).

77. A. Hjorth Larsen *et al.*, The atomic simulation environment—A Python library for working with atoms. *J. Phys. Condens. Matter* **29**, 273002 (2017).
78. S. R. Bahn, K. W. Jacobsen, An object-oriented scripting interface to a legacy electronic structure code. *Comput. Sci. Eng.* **4**, 56–66 (2002).
79. P. Giannozzi *et al.*, QUANTUM ESPRESSO: A modular and open-source software project for quantum simulations of materials. *J. Phys. Condens. Matter* **21**, 395502 (2009).
80. P. Giannozzi *et al.*, Advanced capabilities for materials modelling with Quantum ESPRESSO. *J. Phys. Condens. Matter* **29**, 465901 (2017).
81. A. Togo, First-principles phonon calculations with phonopy and phono3py. *J. Phys. Soc. Japan* **92**, 012001 (2023).
82. A. Togo, I. Tanaka, First principles phonon calculations in materials science. *Scr. Mater.* **108**, 1–5 (2015).
83. K. Czelej, M. R. Zemla, P. Kamińska, P. Śpiewak, K. J. Kurzydłowski, Clustering of hydrogen, phosphorus, and vacancies in diamond: A density functional theory analysis. *Phys. Rev. B* **98**, 075208 (2018).
84. K. Czelej, K. Cwieka, P. Śpiewak, K. J. Kurzydłowski, Titanium-related color centers in diamond: A density functional theory prediction. *J. Mater. Chem. C* **6**, 5261–5268 (2018).
85. R. M. Feenstra *et al.*, Low-energy electron reflectivity from graphene. *Phys. Rev. B* **87** (2013).
86. K. Momma, F. Izumi, VESTA: A three-dimensional visualization system for electronic and structural analysis. *J. Appl. Crystallogr.* **41**, 041406 (2008).
87. K. Momma, F. Izumi, An integrated three-dimensional visualization system VESTA using wxWidgets. *Comm. Crystallogr. Comput. IUCr Newsl.* **7**, 106–119 (2006).
88. K. Momma, F. Izumi, VESTA 3 for three-dimensional visualization of crystal, volumetric and morphology data. *J. Appl. Crystallogr.* **44**, 1272–1276 (2011).
89. A. M. Ganose, A. J. Jackson, D. O. Scanlon, sumo: Command-line tools for plotting and analysis of periodic ab initio calculations. *J. Open Source Software* **3**, 717 (2018).
90. E. Miranda, Phonon website. <https://henriquemiranda.github.io/phononwebsite/phonon.html>. Accessed 14 March 2023.